Journal of Magnetic Resonance 200 (2009) 303–312

Contents lists available at ScienceDirect

Journal of Magnetic Resonance

journal homepage: www.elsevier.com/locate/jmr

Magnetic resonance microscopy of iron transport in methanogenic granules

Jan Bartacek [a,b,*], Frank J. Vergeldt [c], Edo Gerkema [c], Pavel Jenicek [d], Piet N.L. Lens [a,b], Henk Van As [c]

[a] Sub-department of Environmental Technology, Wageningen University, P.O. Box 8219, 6700 EV Wageningen, The Netherlands
[b] Pollution Prevention and Control Core, UNESCO-IHE, P.O. Box 3015, 2601 DA Delft, The Netherlands
[c] Laboratory of Biophysics and Wageningen NMR Centre, Department of Agrotechnology and Food Sciences, Wageningen University, P.O. Box 8128, 6700 ET Wageningen, The Netherlands
[d] Department of Water Technology and Environmental Engineering, Institute of Chemical Technology, Technicka 5, 166 28 Prague 6, Czech Republic

ARTICLE INFO

Article history:
Received 27 February 2009
Revised 10 July 2009
Available online 16 July 2009

Keywords:
Magnetic resonance imaging
Metal diffusion
Biofilm
3D Turbo Spin Echo
Anaerobic granular sludge

ABSTRACT

Interactions between anaerobic biofilms and heavy metals such as iron, cobalt or nickel are largely unknown. Magnetic resonance imaging (MRI) is a non-invasive method that allows *in situ* studies of metal transport within biofilm matrixes. The present study investigates quantitatively the penetration of iron (1.75 mM) bound to ethylenediaminetetraacetate (EDTA) into the methanogenic granules (spherical biofilm). A spatial resolution of $109 \times 109 \times 218\ \mu m^3$ and a temporal resolution of 11 min are achieved with 3D Turbo Spin Echo (TSE) measurements. The longitudinal relaxivity, i.e. the slope the dependence of the relaxation rate ($1/T_1$) on the concentration of paramagnetic metal ions, was used to measure temporal changes in iron concentration in the methanogenic granules. It took up to 300 min for the iron–EDTA complex ($[FeEDTA]^{2-}$) to penetrate into the methanogenic granules (3–4 mm in diameter). The diffusion was equally fast in all directions with irregularities such as diffusion-facilitating channels and diffusion-resistant zones. Despite these irregularities, the overall process could be modeled using Fick's equations for diffusion in a sphere, because immobilization of $[FeEDTA]^{2-}$ in the granular matrix (or the presence of a reactive barrier) was not observed. The effective diffusion coefficient (D_{eff}) of $[FeEDTA]^{2-}$ was found to be $2.8 \times 10^{-11}\ m^2\ s^{-1}$, i.e. approximately 4% of D_{eff} of $[FeEDTA]^{2-}$ in water. The Fickian model did not correspond to the processes taking place in the core of the granule (3–5% of the total volume of the granule), where up to 25% over-saturation by iron (compare to the concentration in the bulk solution) occurred.

1. Introduction

Most of the recent installations for anaerobic wastewater treatment employ methanogenic granules to produce methane and carbon dioxide from the dissolved organic compounds contained in the wastewaters [1]. Methanogenic granules are spherical biofilms, developed spontaneously without support material [2]. The main advantages of this type of biomass are high methanogenic activities and good settling properties enabling reactors employing granular biomass to operate at high volumetric loading rates [3]. The microorganisms forming anaerobic granules need (besides macro-nutrients) sufficient supply of micro-nutrients such as iron, cobalt and nickel [4].

As the physical–chemical interactions between these micro-nutrients (trace metals) and the spherical biofilm matrix are largely unknown and difficult to investigate [5], a suitable measuring technique is required to describe the transport of metals within the anaerobic granules. Presently, modeling of metal transport in biofilms is often based on indirect measurements in the bulk liquid [6]. *In situ* metal concentrations can be measured by microelectrodes, but these microelectrodes are poorly developed [7]. Magnetic Resonance Imaging (MRI) can measure metal transport in porous matrixes non-destructively and non-invasively based on changes in spin–lattice (T_1) or spin–spin (T_2) relaxation times due to the presence of paramagnetic metal ions [8–13]. Although MRI measurements have often been applied to reveal structural and diffusional properties of microbial biofilms [14–19], only a few studies have focused on metal–biofilm interactions [20–24]. A pioneering study was presented by Nestle and Kimmich [25], measuring metal sorption in well defined, highly homogeneous alginate gels and immobilized cells. Similar studies were performed in sandy aquifers [12] and catalyst bodies [13]. Most recently, Phoenix and Holmes [24] presented a MRI study on copper immobilization in phototrophic biofilm.

In the present study, a novel MRI method to quantify metal transport in anaerobic granular sludge was developed. Single methanogenic granules were exposed to an $[FeEDTA]^{2-}$ solution and the consequent penetration of iron into the granule was

* Corresponding author. Address: Pollution Prevention and Control Core, UNESCO-IHE, P.O. Box 3015, 2601 DA Delft, The Netherlands. Fax: +31 (0) 152122921.
E-mail address: j.bartacek@unesco-ihe.org (J. Bartacek).

1090-7807/$ - see front matter © 2009 Elsevier Inc. All rights reserved.
doi:10.1016/j.jmr.2009.07.013

followed in time using T_1 weighted 3D Turbo Spin Echo (TSE) methods [9,26,27]. Using 3D TSE, a spatial resolution of $109 \times 109 \times 218\ \mu m^3$ and a temporal resolution of 11 min was achieved. A method to recalculate the obtained intensity data to real iron concentrations is also presented, from which *in situ* iron concentrations and gradients can be derived.

2. Materials and methods

2.1. Source of biomass

Mesophilic methanogenic granular sludge was obtained from a full-scale UASB reactor treating alcohol distillery wastewater at Nedalco (Bergen op Zoom, The Netherlands).

2.2. Experimental set-up and iron solution

Diffusion measurements were done in an experimental set-up consisting of a storage vessel containing 1 L of measuring solution connected to a measuring tube (inner diameter of 4 mm), in which a single methanogenic granule was immobilized with glass wool. The measuring tube was placed in the imager (Fig. 1). The iron solution was re-circulated by means of a peristaltic pump (Watson-Marlow, Wilmington, USA) to assure steady state conditions outside the granule. The initial images were taken after equilibration with demineralized water. Subsequently, the iron concentration was increased by injection of a concentrated stock solution of $[FeEDTA]^{2-}$ into the storage vessel.

The observed relaxation rates $(1/T_1)$ and $(1/T_2)$ depend linearly on the concentration of paramagnetic metals in the local environment [28]:

$$\frac{1}{T_i} = \left(\frac{1}{T_i}\right)_D + R_i \cdot c_{Me} \quad i = 1,2 \tag{1}$$

where $(1/T_i)_D$ is the diamagnetic (solvent) relaxation rate (in the absence of paramagnetic ions), R_i the relaxivity constant of paramagnetic ions and c_{Me} is the concentration of the paramagnetic metal species. A T_1 relaxivity (R_1) of 1.1 L $mmol^{-1}$ s^{-1} was obtained from a calibration series (concentration range 0.0–2.5 mmol L^{-1}, $R^2 = 0.98$; data not shown). Subsequently, $[FeEDTA]^{2-}$ solutions with a total iron concentration of 1.75 mM were applied in the experiments.

The applied iron concentrations were high enough to obtain measurable changes in the MRI signal and low enough to assure that the T_2 of the granules was not shortened below the value (approximately 0.045 ms) where T_2 weighting starts. Iron was dosed chelated by EDTA to prevent iron from precipitation or sorption on the surface or inside the granular matrix. The solutions were prepared using demineralized water, $FeCl_2{\cdot}4H_2O$ and $Na_2H_2EDTA{\cdot}2H_2O$. The presence of small amounts of free $[H_2EDTA]^{2-}$ in the $[FeEDTA]^{2-}$ solution without an excess of iron can substantially increase the T_1 and T_2 values of the granular matrix (data not shown). Therefore, $FeCl_2{\cdot}4H_2O$ was dosed in 30% excess (i.e. the molar ratio between Fe and EDTA was 1.3:1) in order to avoid interactions between the granular matrix and free EDTA. NaOH was used to adjust the pH to 7.0.

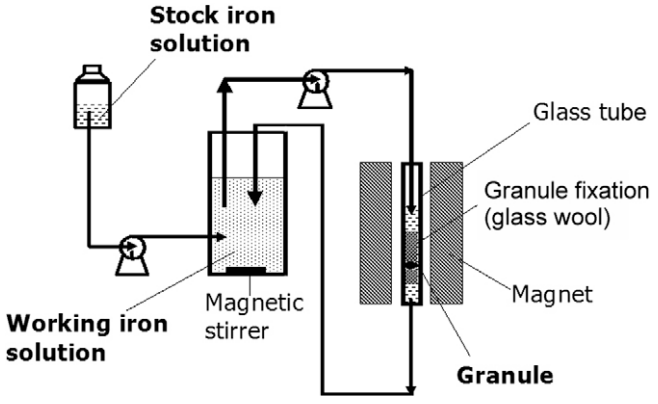

Fig. 1. Experimental set-up used for the $[FeEDTA]^{2-}$ diffusion experiments.

2.3. Nuclear magnetic resonance

2.3.1. ^{1}H-relaxometry

^{1}H-relaxometry was performed on a NMR spectrometer controlled by a Maran Ultra console (Resonance Instruments Ltd., Witney, UK), with a 0.7 T permanent magnet (30.9 MHz proton resonance frequency). Both T_1 and T_2 were measured simultaneously in a combined Inversion Recovery Carr–Purcell–Meiboom–Gill (IR-CPMG) pulse sequence. The inversion time was incremented logarithmically from 2.5 ms up to 10 s in 12 steps. Each CPMG decay train consisted of 16,384 echoes of eight data points each, separated by an echo time of 1 ms. Data were averaged over eight scans with a repetition time of 12.5 s. After careful phase correction of each decay train, each echo was reduced to one averaged data point. The resulting CPMG decay curves were analyzed globally as a sum of exponentials with coupled T_2 values using SPLMOD [29,30]. The amplitudes of the largest component were subsequently analyzed by a function describing inversion recovery to obtain T_1. The data analysis was done using IDL (Research Systems Inc., Boulder, CO, USA).

2.3.2. MRI imager

All MRI measurements were done at 30 (±2) °C on a 0.7 T (30.7 MHz for protons) imager consisting of a Bruker Avance console (Bruker BioSpin, Karlsruhe, Germany), a Bruker electromagnet stabilized by an external ^{19}F lock unit, a custom build solenoid RF-probe and an actively shielded gradient system with planar geometry (G_{max} 1 T/m; Resonance Instruments Ltd., Witney, UK). The RF-probe had an inner diameter of 5 mm and was inductively coupled to avoid continuous retuning and matching of the RF-probe due to the change in loading by the iron solution.

2.3.3. MRI measurements

The Turbo Spin Echo (TSE) measurement was performed as described by Mohoric et al. [27]. The typical acquisition parameters were: repetition time (T_R) 200 ms, echo time (T_E) 4.53 ms, Turbo factor of 4 and 16 averages. The total experiment time was 11 min.

Quantitative 3D amplitude (A_0) and spin–spin relaxation time (T_2) maps were obtained using a Multi-Spin Echo (MSE) measurement [26]. Typical acquisition parameters were: 64 echoes with a T_E of 4.53 ms, T_R 1 s and 4 averages. The total experiment time was 80 min.

3D T_1 and A_0 maps were obtained from Inversion Recovery 3D TSE measurements (IR-TSE). Acquisition parameters were: T_R 7 s, T_E 5.33 ms, TSE factor 8, inversion delay times 0.1, 0.2, 0.4, 1.6, 3.2 and 6.4 s and 2 averages. The total experiment time was 160 min.

The experiments consisted of a series (several tens to several hundreds) of TSE measurements. 3D T_2 and amplitude (A_0) maps of the granule were acquired prior and upon termination of each experiment. The iron solution was always injected after taking several TSE images of the granule in demineralized water to document the situation at time zero. 3D T_1 maps were occasionally acquired due to their long acquisition time requirement (approx. 160 min). Consequently, a series of 3D TSE measurements (30–400) was performed followed always by a final 3D T_2 map measurement.

2.3.4. Spatial resolution

All the imaging procedures (T_1, T_2 and TSE measurements) were done in a 3D mode according to Mohoric et al. [27] with a field of view of $14 \times 4.36 \times 4.36\ mm^3$ ($128 \times 40 \times 20$ voxels) corresponding to a spatial resolution of $0.109 \times 0.109 \times 0.218\ mm^3$.

2.3.5. T_R and T_E adjustment

The signal intensity obtained from the TSE measurement is a function of both the T_1 and T_2 as expressed by [27]:

$$S = A_0\left[1 - \exp\left(-\frac{T_R}{T_1}\right)\right]\exp\left(-\frac{T_E}{T_2}\right) \quad (2)$$

where S is the signal intensity and A_0 the intensity (amplitude) of the signal at time zero (a measure of proton density). The ratio S/A_0 is often referred to as a normalized signal. The signal intensity is influenced by the presence of paramagnetic metals as Eq. (1) implies.

To decide for T_1 or T_2 weighting, the effect of $[FeEDTA]^{2-}$ on the T_1 and T_2 distribution over the methanogenic granule was studied. As shown in Fig. 2, the effect on T_1 inside the granule was substantial, whereas the effect on T_2 was relatively small. Therefore, it was decided to use T_1 weighting and a short T_E of 4.53 ms. In that case, Eq. (1) can be simplified to:

$$S = A_0\left[1 - \exp\left(-\frac{T_R}{T_1}\right)\right] \quad (3)$$

Generally, T_2 only influences the signal intensity when it is close to T_E (approximately $T_2 < 5T_E$). Therefore, the impact of T_2 can be diminished using a short T_E (in the order of milliseconds or less).

Subsequently, optimization of T_R was performed. The maximal difference, i.e. the maximal contrast, can be obtained for T_1-weighted images, when T_R is calculated according to:

$$T_R = \frac{\ln(T_{1,2}/T_{1,1})}{1/T_{1,1} - 1/T_{1,2}} \Rightarrow \frac{S_2 - S_1}{A_0} = \max \quad (4)$$

$T_{1,1}$ and $T_{1,2}$ are the average T_1 values measured, respectively, at the start and the end of the experiment. The optimal T_R value of 347 ms for the granule depicted in Fig. 2 was calculated using Eq. (4). However, to achieve the maximal contrast for the highest concentrations, a lower T_R value (200 ms) was used as calculated from Eq. (5).

$$T_R = 2 \cdot T_1 \Rightarrow \frac{d(S/A_0)}{dT_1} = \max \quad (5)$$

2.4. Image analysis

Data obtained by analysis of every single voxel are presented in this study. The data measured at single voxel level allowed to judge on homogeneity of the granular matrix and on the qualitative aspects of iron transport (homogeneity in all directions, correlation between granular structure and diffusion pattern). These data were, however, too noisy to be used for quantitative calculations (data not shown). Therefore, averaged data were used for quantification of iron diffusion.

To evaluate the 3D images obtained from the MRI measurements (Fig. 3A), the granule was selected by thresholding (Fig. 3B), the binary images were segmented and finally, the signal intensity was measured. Thresholding was based on the signal intensity contrast between the granule and the bulk solution in the TSE image prior to the iron injection (Fig. 3B). The raw binary images were treated by applying the mathematical operations "closing" and "opening" (Fig. 3C). Consequently, the binary image of the granule was segmented into layers of 1 voxel thickness and the average intensity profiles were obtained by averaging the signal intensity over single layers. Because the dimensions of the voxels were asymmetric ($0.109 \times 0.109 \times 0.218\ mm^3$), the images were resized (to voxel dimensions $0.109 \times 0.109 \times 0.109\ mm^3$) using bilinear interpolation prior to the automatic procedure for calculation of the averaged profiles. In this way, images consisting of $128 \times 40 \times 40$ voxels were obtained.

3. Results

3.1. Iron transport within the granular matrix

3.1.1. Changes in signal intensity after iron injection

The signal intensity at the beginning of the experiments (prior to iron injection) was not homogenously distributed over the granule (Fig. 4A), mainly due to heterogeneities in the T_1 values (Fig. 4B). In contrast, the T_2 values and the A_0 values (proton density) were distributed rather homogeneously (Fig. 4C and D, respectively).

Fig. 5A shows the increase of signal intensity after exposure of the granule to a 1.75 mM $[FeEDTA]^{2-}$ solution. The signal intensity reached a plateau in the outer layers and in the core after, respectively, 20 and 300 min following the iron injection (Fig. 5A). The overall difference between the start and the end values were substantially different for single layers.

3.1.2. Calculation of T_1 maps

The T_1 maps (Fig. 6) were calculated from the intensities of the TSE images using Eq. (4) during the entire experiment in order to calculate the actual iron concentration. The A_0 maps needed for this calculation were obtained from the T_2 measurements. The T_1 maps calculated from the TSE measurements (Fig. 6B) were compared with the T_1 maps obtained by direct T_1 measurements done

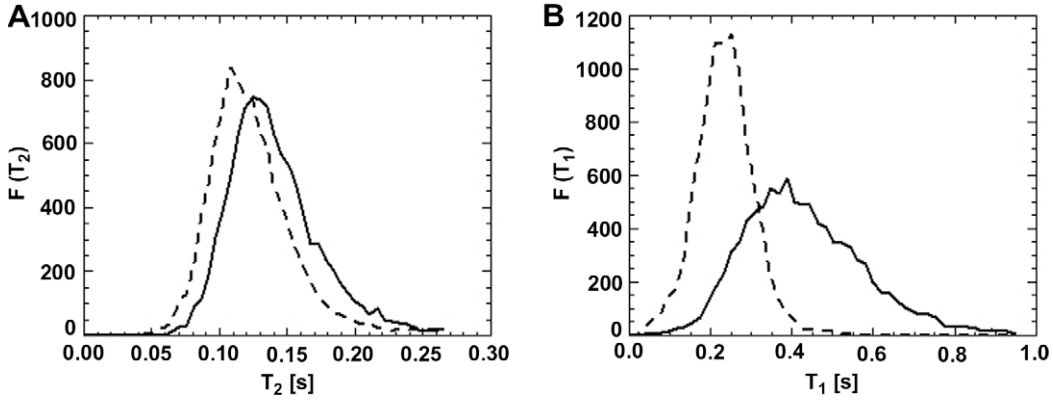

Fig. 2. Distribution of T_2 (A) and T_1 (B) over a single methanogenic granule prior (solid line) and after (dashed line) 15 h exposure to a 1.75 mM $[FeEDTA]^{2-}$ solution. The frequency function ($F(T_i)$) is expressed in number of voxels.

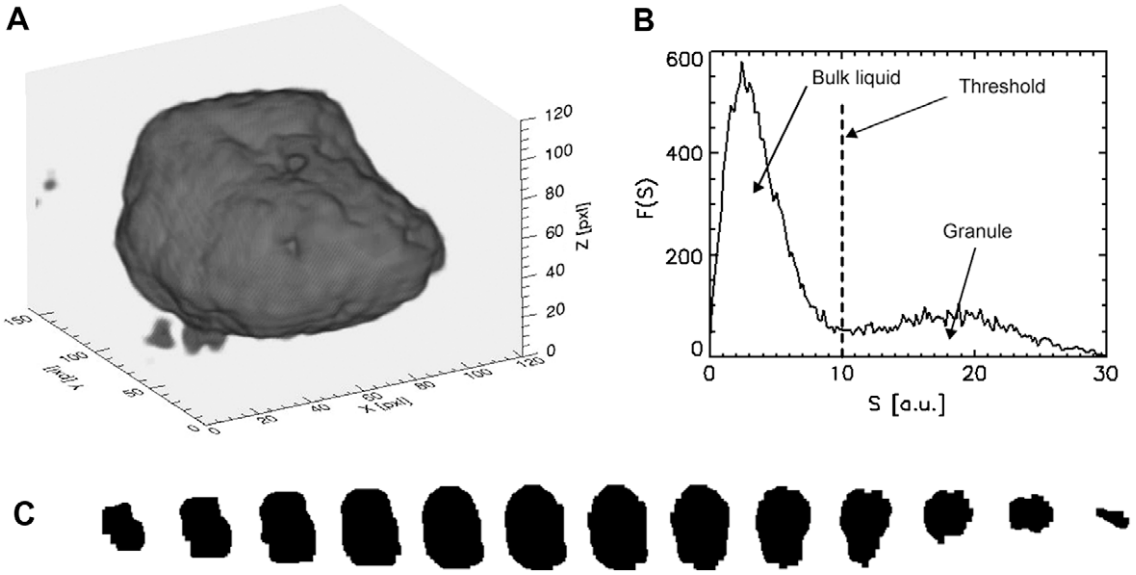

Fig. 3. Segmentation of an initial 3D TSE image based on the signal intensity. Original 3D TSE image (A), histogram of the image (B), binary image (single slices in x–y plain) obtained by thresholding and subsequent application of mathematical operations "closing" and "opening" (C).

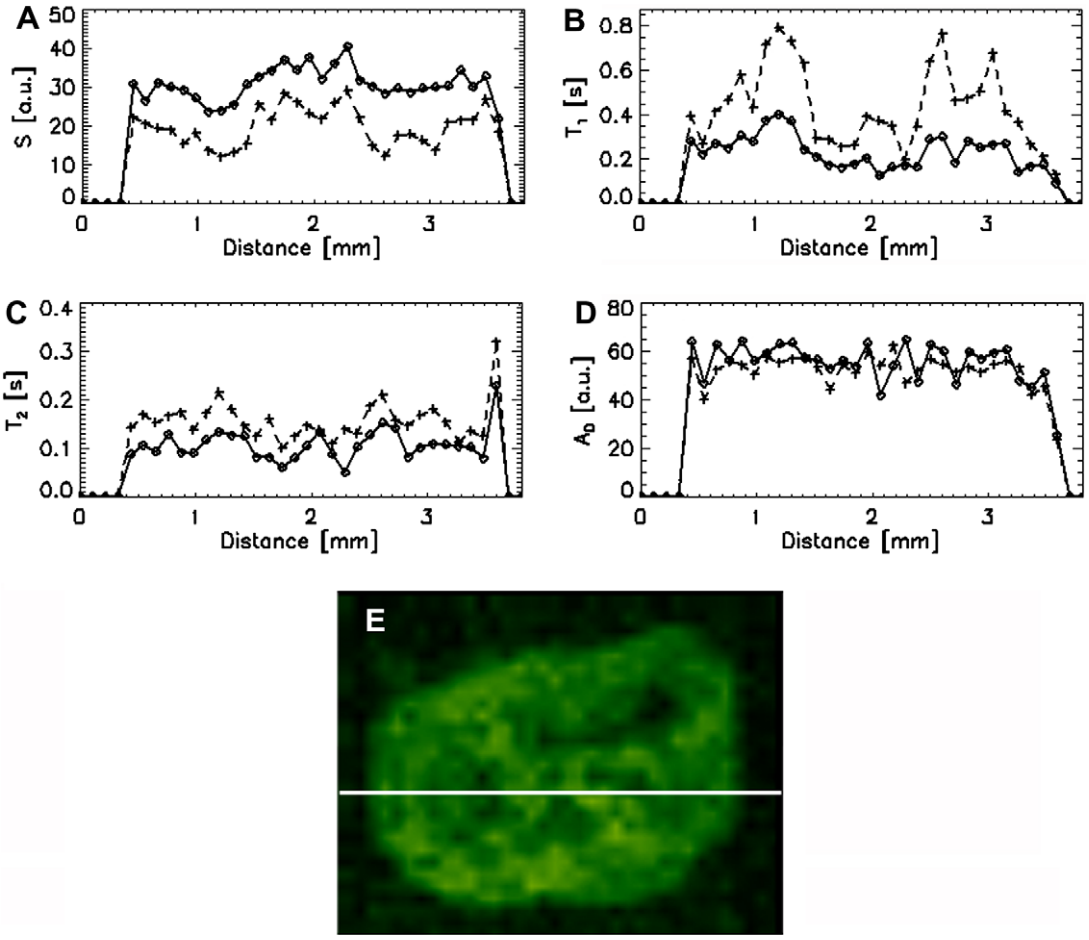

Fig. 4. Single profile over the methanogenic granule at the start (+) and the end (◇) of the experiment. Effect on T_2 (A), T_1 (B), signal intensity (C) and A_0 (D). Illustration of the cross-section in the signal intensity image (E).

at the start of the experiment (Fig. 6A). The measured and calculated T_1 maps were in a good agreement (Fig. 6C), which enabled the further calculation of the iron concentration inside the granule.

3.1.3. Calculation of the iron concentration in granular matrix

Fig. 5B shows the increase of iron concentration in the granule. The iron concentration at a particular time was calculated from Eq. (6) that can be obtained combining Eqs. (3) and (1):

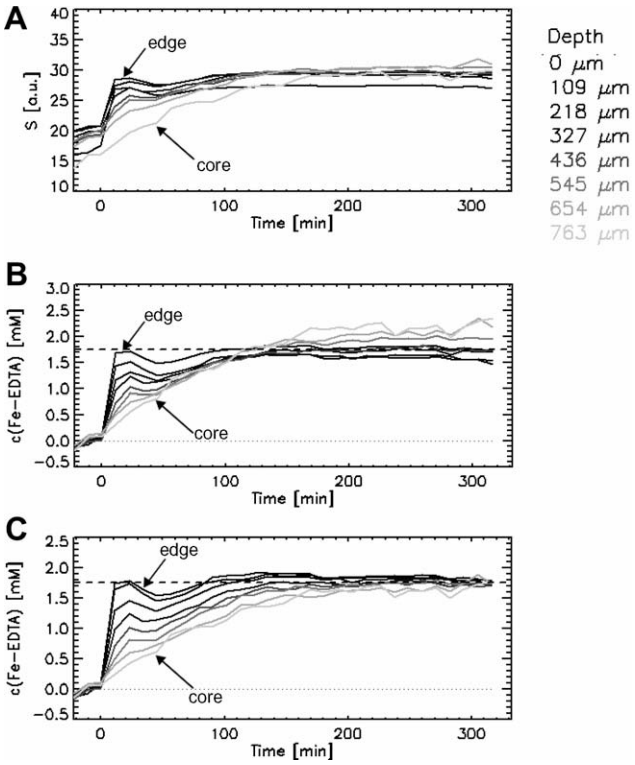

Fig. 5. Effect of iron penetration into a single methanogenic granule. Single curves depict average values for a certain depth from 0 μm (edge) to 763 μm (core). Iron was injected at time 22 min. Signal intensity obtained from the TSE measurement (A), iron concentration calculated using calibration in $[FeEDTA]^{2-}$ solution (B) and relative iron concentration (C). The dashed line indicates the concentration of iron in the bulk solution (B) or the final iron concentration (C).

$$c(\mathrm{Fe}) = -\frac{1}{T_R \cdot R_1} \cdot \left[\ln\left(1 - \frac{S}{A_0}\right) - (1/T_1)_D\right] \quad (6)$$

The value of $(1/T_1)_D$ was irrelevant for the MRI measurements in methanogenic granules, because the T_1 measured in the granular matrix is affected by the biofilm matrix (presence of microorganisms, extracellular polymers (EPS), precipitates, etc.) already prior to the injection of iron. Therefore, $(1/T_1)_D$ was replaced with $1/T_{1,1}$ (relaxation rate at time zero). The value of $1/T_{1,1}$ was determined for each single voxel from TSE measurements and A_0 maps using Eq. (3). The iron concentration was calculated assuming that the T_1 values within the granule change only due to the increase in iron concentration. The final iron concentration was approximately equal to the concentration of the surrounding solution (1.75 mM) in most of the regions inside the granule with higher (up to 2.25 mM) values in the core of the granule.

3.1.4. Heterogeneous iron diffusion within the granular matrix

Iron diffused within the granule at a similar rate in all directions (Fig. 7). However, also channels facilitating the iron transport were present (Fig. 7). Note that the iron concentration increased faster in these channels. The increase in iron concentration was very fast in the core of the granule in all granules studied. Moreover, resistant zones, where the iron concentration increased slower or did not increase at all were also observed in all granules investigated (Fig. 7). The diffusion-resistant zones could be often related to the areas with low-T_1 values (Fig. 8) indicating that the diffusion-resistance occurs especially in the dense area. In contrast, the iron concentration increased faster in the areas with higher T_1 values.

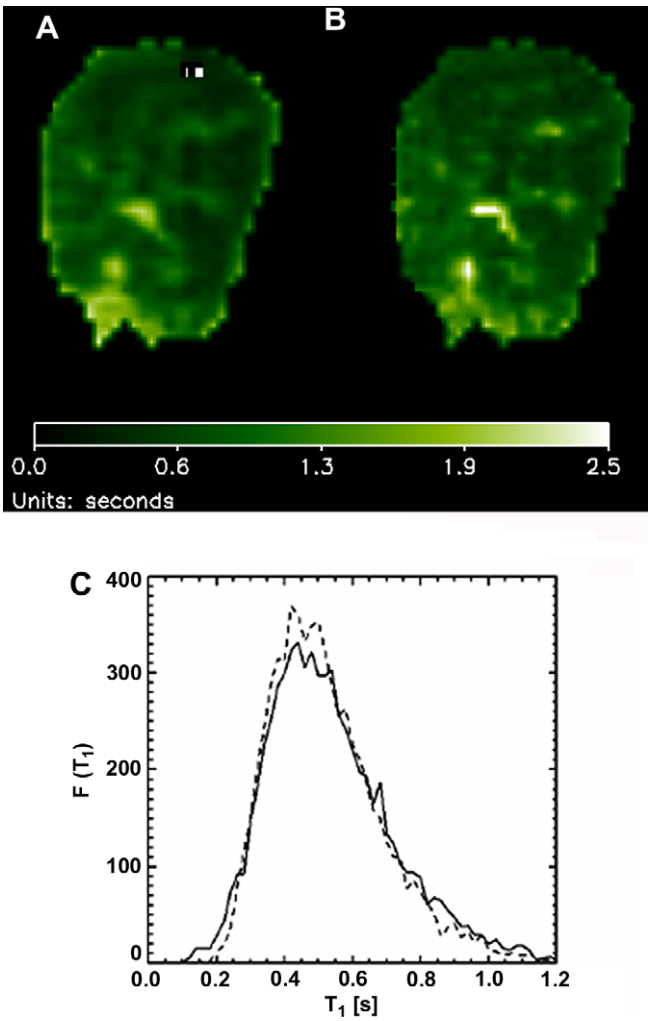

Fig. 6. T_1 map (single cross-section) measured directly (A) and calculated from TSE image and Amplitude map (B) of a single methanogenic granule. Histogram of the measured (solid line) and the calculated (dashed line) T_1 maps (C).

3.1.5. Averaging of the iron concentration data over layers of defined depth

Averaging of the measured data was necessary to describe a quantitative increase of the iron concentration at a given depth in the granule (Fig. 5). Fig. 9 shows the increase of the iron concentration in the same granule as shown in Fig. 7 after averaging of the concentration values over layers of defined depth. The general pattern of the iron diffusion process is preserved (compared to the original values in Fig. 7), but some important details (facilitating channels, resistant zones) were lost by the averaging. The standard deviation of the concentration value calculated for the single layers (calculated to express the heterogeneity of the iron concentration values over one layer) amounted usually up to 40% of the median value (Fig. 10).

3.1.6. Calculation of the average diffusion coefficient in the granule

In order to enable calculation of the diffusion coefficient in the granule using the Fick's diffusion laws, the concentration values were normalized to reach a uniform (1.75 mM) final iron concentration in all layers (Fig. 5C). This process affected only the inner 10% of the total volume of the granule. Consequently, theoretical calculations of the diffusion coefficient were performed using Eq. (7), which is derived from Fick's diffusion laws in a sphere:

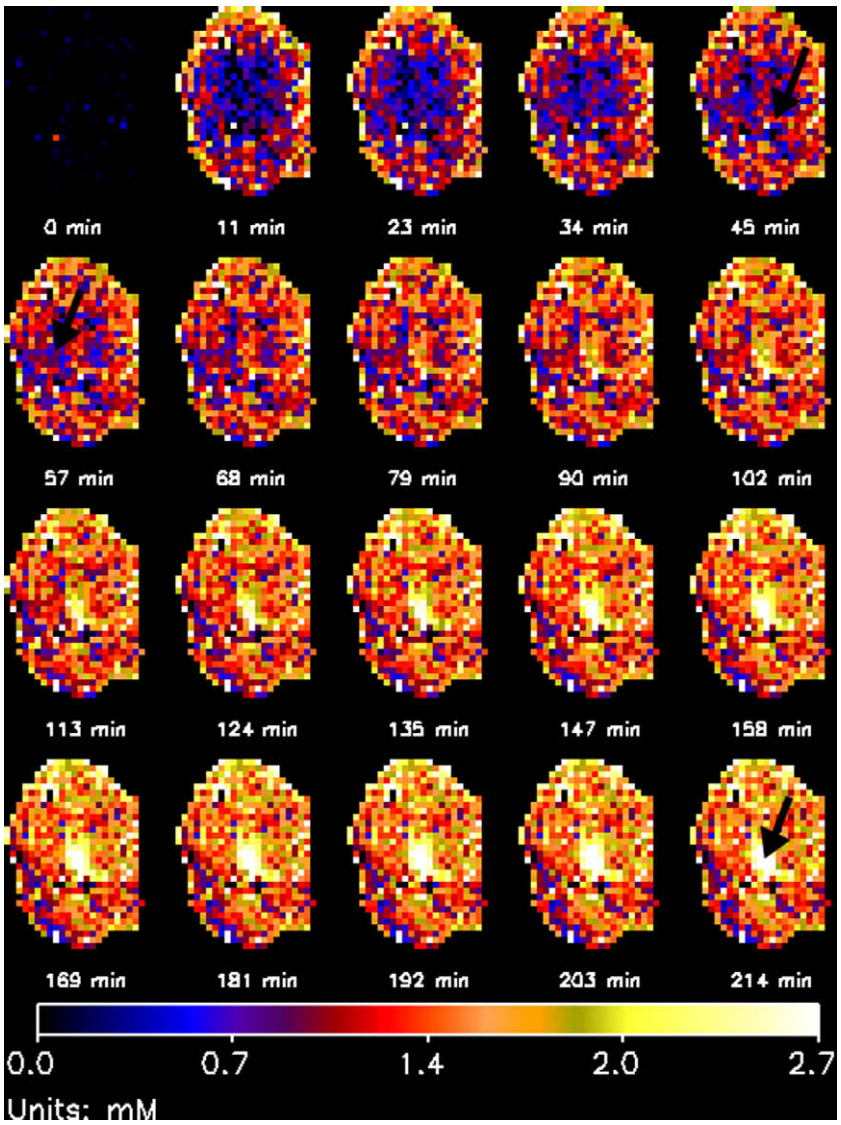

Fig. 7. Iron diffusion into a single methanogenic granule exposed to 1.75 mM $[FeEDTA]^{2-}$ solution. The color bar at the bottom shows the iron concentration in mM. The black arrows in the figure at time 45, 57 and 214 min indicate the transport facilitating channel, transport resistant zone and the core with higher final concentration, respectively.

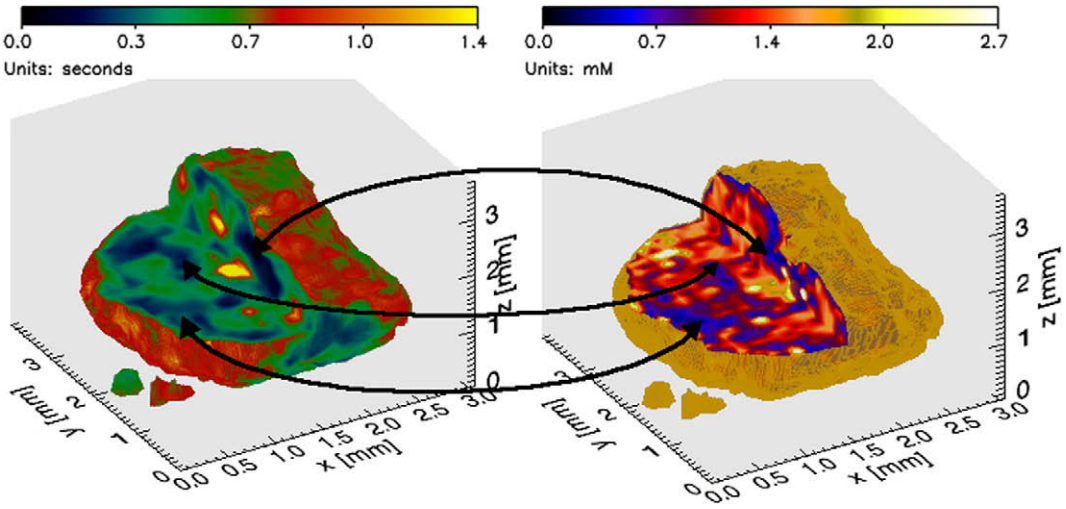

Fig. 8. Partial cross-section through the methanogenic granule, with T_1 values (left) and iron concentration at time 57 min (right) visualized. The arrows connect the low-T_1 zones with the corresponding diffusion-resistant zones. The volumetric images were magnified using linear interpolation.

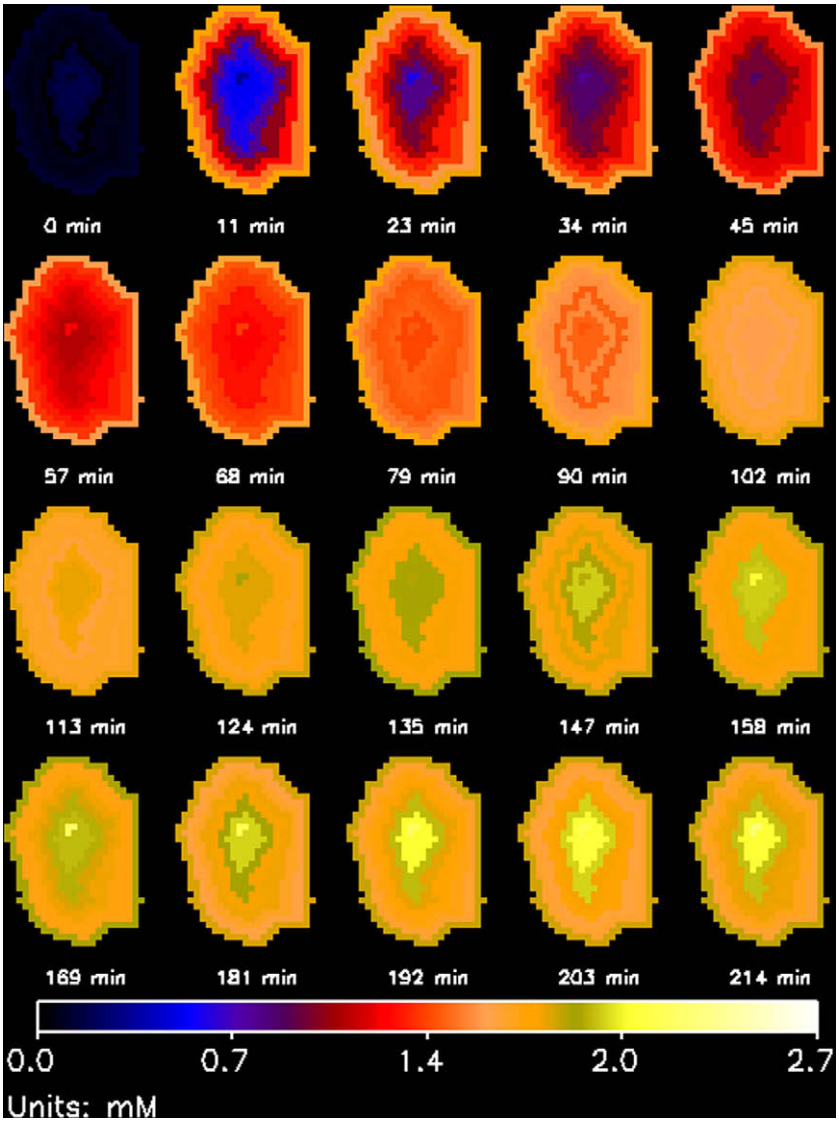

Fig. 9. Iron diffusion into a single methanogenic granule, when the concentration values were averaged over 109 μm thick layers.

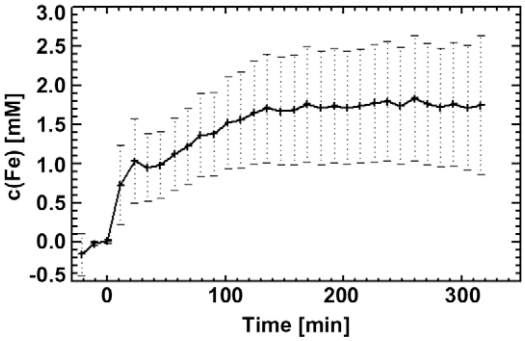

Fig. 10. Increase of the average iron concentration in one layer (depth 0.327 mm). The error bars represent the heterogeneity (calculated as standard deviation within the layer) of the iron concentration over the layer.

$$\frac{c(\mathrm{Fe})-c(\mathrm{Fe})_{\mathrm{start}}}{c(\mathrm{Fe})_{\mathrm{end}}-c(\mathrm{Fe})_{\mathrm{start}}}=1+\frac{2r_0}{\pi r}\sum_{n=1}^{\infty}\frac{(-1)^n}{n}\times\sin\left(\frac{\pi n r}{r_0}\right)\exp\left(-\frac{\pi^2 n^2 D t}{r_0^2}\right) \quad (7)$$

where D is the diffusion coefficient, t is the time after iron injection and r_0 is the theoretical radius of the granule (the granule is considered to be spherical). Fig. 11A shows the fitting of the experimental data with the theoretical model represented by Eq. (7). For this purpose, the averaged concentration profiles (as represented in Fig. 5) were used. Applying Eq. (7), a diffusion coefficient of $2.8\times10^{-11}\ \mathrm{m^2\,s^{-1}}$ was obtained. The value of D was determined to minimize the sum of the squared errors for all layers.

Coefficients of determination (R^2) between the experimental and theoretical data calculated for single layers were in the range of 0.92–0.99, with an exception for the layer representing the core of the granule (correlation coefficient 0.76). While the fitting is almost perfect for the outer three layers, there is some deviation from the theory in the inner four layers. In the latter layers, the iron concentration increase was faster than the theory in the first 30–40 min and slower than the theory in the later period (50–300 min).

Fitting of the experimental data that were not normalized with the uniform final iron concentration (as shown in Fig. 5B) was also performed using Fick's diffusion laws (Fig. 11B). Although Fick's laws do not consider a non-equal distribution of the final solute concentration over the sphere, the coefficients of determination

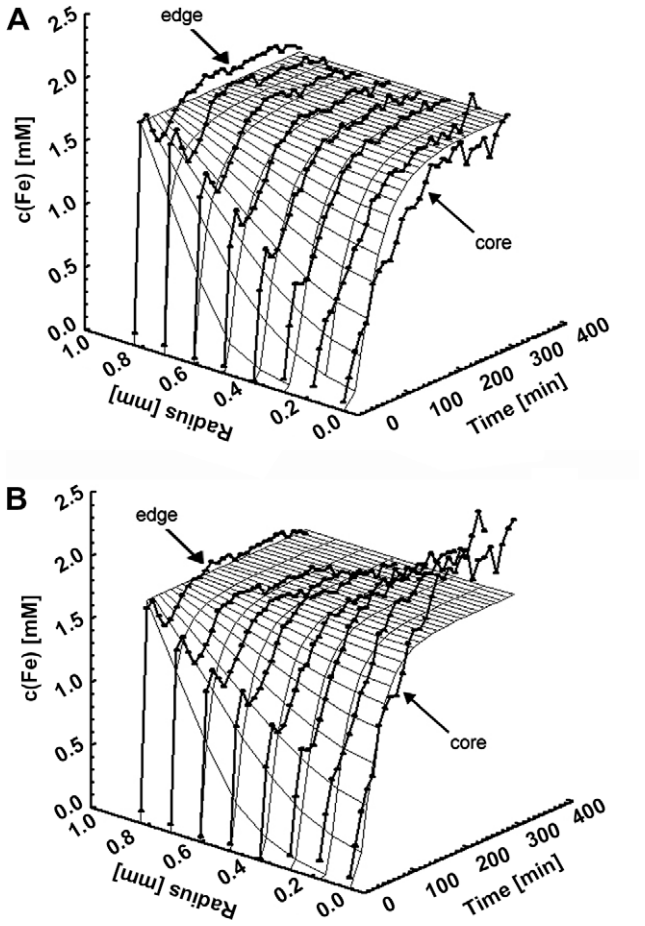

Fig. 11. Comparison of the theoretical values obtained applying the Fick's laws for diffusion in a sphere (gray wire net) with the measured iron concentration (black lines with data points) normalized to reach the final iron concentration of 1.75 mM (A) and without normalization (B).

ranged from 0.93 to 0.96. The diffusion coefficient calculated in this way was 3.5×10^{-11} m^2 s^{-1}.

4. Discussion

This study demonstrates a new MRI method for transport studies of paramagnetic metals in methanogenic (granular) biofilms. The TSE MRI technique was used for a near real-time observation of iron penetration into a single methanogenic granule.

4.1. Diffusion pattern in the methanogenic granule

Fig. 7 shows that the overall iron penetration was equal in all directions. However, fine structures (facilitating channels and resistant zones) that affect the iron transport within the granular matrix were detected (Fig. 7). The iron concentration increased faster in the facilitating channels and slower (or not at all) in the resistant zones (Fig. 8). Although the values of T_1 measured in these channels (typically 0.4–0.7 s) were higher than the T_1 values of the diffusion-resistant zones (typically 0.1–0.3 s), the T_1 of free water is still much higher (more than 4 s). This indicates that the facilitating channels were not cracks (or vents) filled with water. The water filled cracks were observed in the core of several methanogenic granules under study (data not shown), but these were not connected to the bulk liquid and did not contribute substantially to the transport of the iron complex. Note that the cracks in the core can develop, e.g. due to biomass decay during a starvation period [14] and are thus not primarily formed to facilitate transport processes within the biofilm matrix. The observation of that one or two cracks per a biofilm sample that did not influence the metal transport was also reported by Phoenix and Holmes [24] in phototrophic biofilm suggesting that the development of these cracks is a common feature for biofilms.

Nestle and Kimmich [25,31,32] and Nestle [8] observed the existence of a reactive barrier when studying metal absorption in alginate biosorbents and immobilized cells. Such an effect was not observed in the present study. In contrast, the iron concentration increased in the core of the granule immediately after the iron injections. This was most probably enabled by the presence of the facilitating channels (Figs. 7 and 8).

The uniform rate of increase of the iron concentration allowed averaging of the iron concentration at a particular time over layers of defined distance from the surface of the granule. Fig. 9 shows that the general pattern of increase of the iron concentration in the granule was preserved by the averaging. However, the averaging neglected the existence of the fine structures inside the granule (channels and resistant zones). The latter was quantitatively expressed by the relatively high heterogeneity of the iron concentration values at each layer (Fig. 10).

4.2. Modeling of the iron diffusion process

The shrinking core model (SCM) [32] has been previously used for modeling of the penetration of metals into a biofilm. Phoenix and Holmes [24] used a similar model. Both models include sorption of metals in the biofilm inducing the formation of a reactive barrier inside the biofilm [32]. In the present study, the sorption/precipitation of iron was partially avoided by dosing iron bound to EDTA, and the presence of the reactive barrier was not observed indicating that the diffusion process can be modeled by Fickian diffusion in a sphere. Unavoidably, free iron (Fe^{2+}) present in a 30% excess (i.e. the molar ratio between Fe and EDTA was 1.3:1) in the $[FeEDTA]^{2-}$ solution could partially precipitate in the granule.

The models that have been used for metal diffusion in biofilms such as the SCM [32] or Bartlett and Gardner model [24] consider an equal distribution of the final metal concentration in the biofilm. Indeed, this is also the case for Fick's diffusion laws used in this study. The equal distribution of the final metal concentration was not observed in this study (Fig. 11B) (also in [24]). Therefore, the raw iron concentration data were normalized to reach an equal final value (1.75 mM) prior to fitting with the model (Fig. 11A). In this way, the result (D_{ejf}) is not influenced by the accumulation of iron in the core of the granule, which represents less than 5% of the total volume of the granule.

An effective diffusion coefficient (D_{ejf}) of 2.8×10^{-11} m^2 s^{-1} was obtained for iron diffusion within the methanogenic granules used in this study. This value is approximately 4% of the diffusion coefficient of $[FeEDTA]^{2-}$ that was measured in aqueous solutions (0.58×10^{-9} m^2 s^{-1}) [33]. The latter observation is consistent with the results of Kitsos et al. [34], who observed a 7% D_{ejf} of lithium (Li^+) in methanogenic biofilms compared to the D_{ejf} of lithium in water.

D_{ejf} of water has been previously investigated in comparable methanogenic granules as used in the present study and it ranged from 70% to 80% of D_{ejf} in free water [14], suggesting that the D_{ejf} of metals in biofilms is restricted more than the D_{ejf} of water. The value of D_{ejf} in biofilms depends on the physical–chemical properties of both the solute and biofilm [35]. A relatively large hydrodynamic radius of the $[FeEDTA]^{2-}$ complex compared to that of free metal ions [33] (and certainly much larger than hydrodynamic radius of water) can be one of the properties substantially decreasing the D_{ejf} of $[FeEDTA]^{2-}$ in the biofilm.

4.3. MRI for metal transport studies

A 3D TSE method optimized for measurement of the metal ion concentrations in methanogenic granules was used in the present study to achieve sufficient spatial and temporal resolution. The basic concepts were adopted from the pioneering work by Nestle and Kimmich [25,31,32] and Nestle [8]. Alternative MRI methods are available such as spin echo (SE) [10,11], fast low angle shot (FLASH) [9,11] and gradient echo (GE) [9] imaging. Generally, the FLASH and TSE sequences have the advantage of much lower time demand over the SE and GE sequences.

The GE method is insufficient for metal transport measurements due to a low signal-to-noise ratio [9]. FLASH offers a high contrast for different metal concentrations [9,11]. However, the method is very sensitive to distortion of the signal by the presence of paramagnetic particles [11]. Nestle et al. [11] overcame the latter problem by using the SE method, but this was at the expense of a lower contrast and lower temporal resolution that hampered quantification of the metal concentration.

TSE was criticized by Moradi et al. [9], because they did not obtain high enough signal at low nickel concentrations (less than 0.5 mM). However, the present study shows that using an appropriate T_R (adjusted for the material under investigation), measuring iron concentrations as low as 0.1 mM is well possible even at a low magnetic field (B_0 = 0.7 T). The upper limit of the iron concentration is given by the ability to use a very short T_E. As documented by the present work for measurements with iron, the TSE method has the advantages of both FLASH and SE: a high contrast between different metal concentrations, a low sensitivity to paramagnetic particles and the signal can be obtained even when the T_1 is relatively high (around 1 s).

4.4. T_1 versus T_2 weighted TSE signal

Recently, Phoenix and Holmes [24] demonstrated a method to measure copper immobilization in photosynthetic biofilms measuring changes in T_2 induced by copper penetration in the biofilm (T_2 weighting). The method presented by them cannot be applied on the measurements in the present study, because it has a too low temporal and spatial resolution. Also Graf von der Schulenburg et al. [23] used T_2 weighting to follow cobalt sorption in a *Serratia* sp. biofilm layer grown on the surface of polyurethane foam in an air-lift fermenter. However, the biofilm in that study was only detected based on a large difference between the T_2 value of the biofilm (approximately 0.4 s) and the T_2 value of the bulk water (approximately 2.1 s). The cobalt concentrations (up to 10 mM) were only measured in the liquid phase, for which the T_2 weighted 2D TSE proved suitable [23]. Also note that Graf von der Schulenburg et al. [23] performed measurements at a magnetic field of 9 T while only 0.7 T was applied in the present study.

It was shown in the present study that the T_2 values within the granule are already low and therefore the changes in T_2 due to iron diffusion are rather small (Fig. 2). Therefore, the T_1 weighting is more suitable than T_2 weighting to determine the metal concentration inside the matrix of the methanogenic granules.

4.5. Determination of iron concentration within the anaerobic granule

The final concentration of iron as measured by MRI was equal to the concentration introduced into the bulk liquid in most of the volume of the granules under investigation. This indicates that the T_1 relaxivity of the $[FeEDTA]^{2-}$ solution measured in free water can be used as a calibration for measurements inside methanogenic granules. An accumulation (up to 125% of the concentration in the bulk liquid) was observed only in the inner three layers representing less than 5% of the overall volume of the granules.

The local accumulation of iron in the core of the granule can result from the presence of a Donnan potential, i.e. the potential causing a distribution of ion species between two ionic solutions separated by a semi-permeable membrane or boundary, in the granular matrix [36]. The negative charge of the complex $[FeEDTA]^{2-}$ should cause rather lower iron concentrations in the matrix, because the charged groups present in the anaerobic granules (and causing the Donnan potential) are usually also negatively charged [7]. However, the free iron (Fe^{2+}) present in 30% excess in the $[FeEDTA]^{2-}$ solution could accumulate in the granule due to the Donnan effect. Note that such over-saturation with Fe^{2+} would cause local changes in iron relaxivity, because free iron (Fe^{2+}) has higher relaxivity than $[FeEDTA]^{2-}$ (data not shown). This effect can cause an overestimation of the iron concentration found in the core of the granule. No sufficient data could be collected for an exact quantification of these effects. However, the importance of the over-saturation is relatively low as it was detected only in a small portion (less than 5%) of the total volume of the granule.

The apparent higher iron concentration in the core of the granule could also be caused by slightly higher iron relaxivity in this area. Phoenix and Holmes [24] observed a linear relation between the water content and copper relaxivity of several biological materials such as different agars or bacterial pellets. However, no correlation between the distribution of the modified iron relaxivity (calculated for the case when the final iron concentration was equal in the whole granule) and A_0 (expressing water density) was found in the present study (data not shown). This indicates that the hypothetical T_1 relaxivity variation within the methanogenic granules did not result from the variation in the water content over the granule.

Acknowledgments

The authors would like to acknowledge Ing. John Philippi for constructing the inductively coupled RF-probe. This work was supported by the European Union via the Research Infrastructure Wageningen NMR Centre (Contract No. 026164 Research Infrastructure Transnational Access WNMRC) to H.V.A., the research grant for Transnational Access to Research Infrastructure Wageningen NMR Centre "MRI Application to measure iron transport in anaerobic granular biofilm" (WNMRC07-006) to J.B., the Marie Curie Training Site "Heavy Metals and Sulfur" (MCFH-1999-00950) to P.N.L.L., the Marie Curie Excellence Grant "Novel biogeological engineering processes for heavy metal removal and recovery" (MEXT-CT-2003-509567) to P.N.L.L. and the Marie Curie Intra European Fellowship "Bioavailability of trace metals in anaerobic granular sludge reactors" (MEIF-CT-2007-041896) to J.B.

References

[1] J.B. Van Lier, Current and future trends in anaerobic digestion: diversifying from waste (water) treatment to resource oriented conversion techniques, in: Proceedings of the 11th IWA-International Conference on Anaerobic Digestion, Brisbane, Australia, 23–27 September, 2007.
[2] L.W. Hulshoff Pol, S.I. de Castro Lopes, G. Lettinga, P.N.L. Lens, Anaerobic sludge granulation, Water Res. 38 (2004) 1376–1389.
[3] G. Gonzalez-Gil, L. Seghezzo, G. Lettinga, R. Kleerebezem, Kinetics and mass-transfer phenomena in anaerobic granular sludge, Biotechnol. Bioeng. 73 (2001) 125–134.
[4] F.G. Fermoso, G. Collins, J. Bartacek, V. O'Flaherty, P.N.L. Lens, Role of nickel in high rate methanol degradation in anaerobic granular sludge bioreactors, Biodegradation 19 (2008) 725–737.
[5] E.D. Van Hullebusch, S. Utomo, M.H. Zandvoort, P.N.L. Lens, Comparison of three sequential extraction procedures to describe metal fractionation in anaerobic granular sludges, Talanta 65 (2005) 549–558.
[6] H. Beyenal, Z. Lewandowski, Dynamics of lead immobilization in sulfate reducing biofilms, Water Res. 38 (2004) 2726–2736.
[7] E.D. Van Hullebusch, M.H. Zandvoort, P.N.L. Lens, Metal immobilisation by biofilms: mechanisms and analytical tools, Rev. Environ. Sci. Biotechnol. 2 (2003) 9–33.

[8] N. Nestle, NMR studies on heavy metal immobilization in biosorbents and mineral matrices, Rev. Environ. Sci. Biotechnol. 1 (2002) 215.
[9] A.B. Moradi, S.E. Oswald, J.A. Massner, K.P. Pruessmann, B.H. Robinson, R. Schulin, Magnetic resonance imaging methods to reveal the real-time distribution of nickel in porous media, Eur. J. Soil Sci. 59 (2008) 476–485.
[10] H. Van As, D. van Dusschoten, NMR methods for imaging of transport processes in micro-porous systems, Geoderma 80 (1997) 389–403.
[11] N. Nestle, T. Baumann, A. Wunderlich, R. Niessner, MRI observation of heavy metal transport in aquifer matrices down to sub-mg quantities, Magn. Reson. Imag. 21 (2003) 345–349.
[12] N. Nestle, A. Wunderlich, R. Niessner, T. Baumann, Spatial and temporal observations of adsorption and remobilization of heavy metal ions in a sandy aquifer matrix using magnetic resonance imaging, Environ. Sci. Technol. 37 (2003) 3972–3977.
[13] J.A. Bergwerff, A.A. Lysova, L. Espinosa Alonso, I.V. Koptyug, B.M. Weckhuysen, Probing the transport of paramagnetic complexes inside catalyst bodies in a quantitative manner by magnetic resonance imaging, Angew. Chem., Int. Ed. 46 (2007) 7224–7227.
[14] P.N.L. Lens, R. Gastesi, F. Vergeldt, A.C. van Aelst, A.G. Pisabarro, H. Van As, Diffusional properties of methanogenic granular sludge: ^{1}H NMR characterization, Appl. Environ. Microbiol. 69 (2003) 6644–6649.
[15] G. Gonzalez-Gil, P.N.L. Lens, A. Van Aelst, H. Van As, A.I. Versprille, G. Lettinga, Cluster structure of anaerobic aggregates of an expanded granular sludge bed reactor, Appl. Environ. Microbiol. 67 (2001) 3683–3692.
[16] Z. Lewandowski, S.A. Altobelli, E. Fukushima, NMR and microelectrode studies of hydrodynamics and kinetics in biofilms, Biotechnol. Progr. 9 (1993) 40–45.
[17] J.S. McLean, O.N. Ona, P.D. Majors, Correlated biofilm imaging, transport and metabolism measurements via combined nuclear magnetic resonance and confocal microscopy, ISME J. 2 (2008) 121–131.
[18] B.C. Hoskins, L. Fevang, P.D. Majors, M.M. Sharma, G. Georgiou, Selective imaging of biofilms in porous media by NMR relaxation, J. Magn. Reson. 139 (1999) 67–73.
[19] M. Vogt, H.C. Flemming, W.S. Veeman, Diffusion in *Pseudomonas aeruginosa* biofilms: a pulsed field gradient NMR study, J. Biotechnol. 77 (2000) 137–146.
[20] J.D. Seymour, S.L. Codd, E.L. Gjersing, P.S. Stewart, Magnetic resonance microscopy of biofilm structure and impact on transport in a capillary bioreactor, J. Magn. Reson. 167 (2004) 322–327.
[21] J.D. Seymour, J.P. Gage, S.L. Codd, R. Gerlach, Magnetic resonance microscopy of biofouling induced scale dependent transport in porous media, Adv. Water Resour. 30 (2007) 1408–1420.
[22] K.P. Nott, M. Paterson-Beedle, L.E. Macaskie, L.D. Hall, Visualisation of metal deposition in biofilm reactors by three-dimensional magnetic resonance imaging (MRI), Biotechnol. Lett. 23 (2001) 1749–1757.
[23] D.A. Graf von der Schulenburg, D.J. Holland, M. Paterson-Beedle, L.E. Macaskie, L.F. Gladden, M.L. Johns, Spatially resolved quantification of metal ion concentration in a biofilm-mediated ion exchanger, Biotechnol. Bioeng. 99 (2008) 821–829.
[24] V.R. Phoenix, W.M. Holmes, Magnetic resonance imaging of structure, diffusivity, and copper immobilization in a phototrophic biofilm, Appl. Environ. Microbiol. 74 (2008) 4934–4943.
[25] N. Nestle, R. Kimmich, NMR imaging of heavy metal absorption in alginate, immobilized cells, and kombu algal biosorbents, Biotechnol. Bioeng. 51 (1996) 538–543.
[26] H.T. Edzes, D. van Dusschoten, H. Van As, Quantitative T2 imaging of plant tissues by means of multi-echo MRI microscopy, Magn. Reson. Imag. 16 (1998) 185–196.
[27] A. Mohoric, F. Vergeldt, E. Gerkema, A. de Jager, J. van Duynhoven, G. van Dalen, H. Van As, Magnetic resonance imaging of single rice kernels during cooking, J. Magn. Reson. 171 (2004) 157–162.
[28] R.B. Lauffer, Paramagnetic metal complexes as water proton relaxation agents for NMR imaging: theory and design, Chem. Rev. 87 (1987) 901–927.
[29] R.W.W. van Resandt, R.H. Vogel, S.W. Provencher, Double beam fluorescence lifetime spectrometer with subnanosecond resolution: application to aqueous tryptophan, Rev. Sci. Instrum. 53 (1982) 1392–1397.
[30] S.W. Provencher, R.H. Vogel, Regularization techniques for inverse problems in molecular biology, in: P. Deuflhard, E. Hairer (Eds.), Numerical Treatment of Inverse Problems in Differential and Integral Equations, Birkhäuser, Boston, 1983, pp. 304–319.
[31] N. Nestle, R. Kimmich, Susceptibility NMR microimaging of heavy metal uptake in alginate biosorbents, Magn. Reson. Imag. 14 (1996) 905–906.
[32] N. Nestle, R. Kimmich, Heavy metal uptake of alginate gels studied by NMR microscopy, Colloids Surf. A: Physicochem. Eng. Aspects 115 (1996) 141–147.
[33] D.G. Leaist, L. Hao, Tracer diffusion of some metal ions and metal–EDTA complexes in aqueous sodium chloride solutions, J. Chem. Soc. Faraday Trans. 90 (1994) 133–136.
[34] H.M. Kitsos, R.S. Roberts, W.J. Jones, T.G. Tornabene, An experimental study of mass diffusion and reaction rate in an anaerobic biofilm, Biotechnol. Bioeng. 39 (1992) 1141–1146.
[35] P.S. Stewart, Diffusion in biofilms, J. Bacteriol. 185 (2003) 1485–1491.
[36] G.H. Dibdin, Mathematical modeling of biofilms, Adv. Dental Res. 11 (1997) 127–132.